Available online at www.sciencedirect.com
SCIENCE DIRECT®
Journal of Solid State Chemistry 178 (2005) 2734–2740
JOURNAL OF SOLID STATE CHEMISTRY
www.elsevier.com/locate/jssc

Sol–gel deposition and luminescent properties of $LaMgAl_{11}O_{19}:Ce^{3+}/Tb^{3+}$ phosphor films

P.Y. Jia, M. Yu, J. Lin*

Key Laboratory of Rare Earth Chemistry and Physics, Changchun Institute of Applied Chemistry, Chinese Academy of Sciences, Changchun 1300; and Graduate School of the Chinese Academy of Sciences, Beijing 100049, PR China

Received 24 January 2005; received in revised form 6 June 2005; accepted 12 June 2005
Available online 27 July 2005

Abstract

Rare earth ions (Ce^{3+}, Tb^{3+})-doped $LaMgAl_{11}O_{19}$ phosphor films were deposited on quartz glass substrates by Pechini sol–gel and dip coating method. X-ray diffraction (XRD), Fourier transform infrared spectroscopy (FT–IR), thermogravimetric and differential thermal analysis (TG–DTA), atomic force microscopy (AFM), field emission scanning electronic microscopy (FESEM), photoluminescence (PL) spectra, and lifetimes were used to characterize the resulting films. The results of XRD indicated that the magnetoplumbite structure $LaMgAl_{11}O_{19}$ phase can be obtained at 1200 °C on quartz glass substrates. This was further verified by the results of FT–IR and TG–DTA. AFM study showed that uniform films have an average grain size of 150 nm and a root mean square (RMS) roughness of 4 nm. The thickness of the films characterized by FESEM is about 340 nm. $LaMgAl_{11}O_{19}:Ce^{3+}$ film showed the parity and spin allowed $5d$–$4f$ band emission of Ce^{3+} with a maximum at 350 nm. Ce^{3+}, Tb^{3+}-codoped $LaMgAl_{11}O_{19}$ films showed the band emission of Ce^{3+} and characteristic emission of Tb^{3+}, namely, $^5D_{3,4}$-^7F_J ($J = 6, 5, 4, 3$) due to an efficient energy transfer from Ce^{3+} to Tb^{3+} in the host.

Keywords: Sol–gel; Luminescence; Rare earth; $LaMgAl_{11}O_{19}$; Phosphor film

1. Introduction

Luminescent materials are applied to displaying faceplates either in powder form or in thin film form. In the first case, the powder phosphors are mixed with organic binders to spread on a substrate, while in the latter case thin film phosphors are deposited on a substrate followed by subsequent annealing. In 1980, Robertson and van Tol [1] found that rare earth-doped garnet luminescent films epitaxially grown on single crystal substrates could withstand much higher power densities than those with powder phosphors without tube degradation. Since then much attention has been paid to thin film phosphors [2–5]. In thin film phosphors, the uniform thickness combined with smoother surface morphology and smaller grain size make it possible for defining smaller pixel spot size to achieve a higher resolution [1,2]. Thin phosphor films can be fabricated by a variety of methods, such as chemical vapor deposition [6], spray pyrolysis [7], pulsed laser deposition [8] and sol–gel [9]. Compared with the other methods, the sol–gel process which uses simple and cheap equipment, is a promising method for film fabrication. In the past decade, sol–gel technology has been employed to fabricate a variety of phosphor films, such as, $Y_3Al_5O_{12}$:Tb [2] films for cathodoluminescence, $Y_3Al_5O_{12}$:Eu [10] and $Y_3(Al, Ga)_5O_{12}$:Tb [11] films for field emission displays, Y_2O_3:Eu [12] and Zn_2SiO_4:Mn [13] films for photoluminescence (PL).

In most of the above-mentioned cases, the sol–gel precursors used are metal alkoxides and/or organmetallic compounds, which suffer from high cost, toxicity and difficulty in controlling the experimental processes.

*Corresponding author. Fax: +86 431 5698041.
E-mail address: jlin@ns.ciac.jl.cn (J. Lin).

0022-4596/$ - see front matter © 2005 Elsevier Inc. All rights reserved.
doi:10.1016/j.jssc.2005.06.019

An alternative approach to form crystalline thin films is the Pechini sol–gel process, which mainly employs inorganic salts as precursors, citric acid as chelate ligand and polyethylene glycol (PEG) as crosslinking agent [14,15].

$LaMgAl_{11}O_{19}$ (LMA), with the magnetoplumbite structure, has been shown to be an important host of rear earth ions. Nd^{3+}-doped LMA crystal have been devoted to laser applications [16]. $Ce_{0.65}Tb_{0.35}MgAl_{11}O_{19}$ is a commercially used green phosphor in fluorescence lamp [17]. As far as we know, so far no phosphor film based on LMA has been reported. Accordingly, in this article we report the preparation of the Ce^{3+}, Tb^{3+}-doped LMA thin phosphor films by Pechini sol–gel method, and investigate their luminescence and energy transfer properties.

2. Experimental section

2.1. Fabrication of $LaMgAl_{11}O_{19}:Ce^{3+}$, Tb^{3+} films and powers

The films of $LaMgAl_{11}O_{19}:Ce^{3+}$ and $LaMgAl_{11}O_{19}:Ce^{3+}$, Tb^{3+} were fabricated by a Pechini sol–gel and dip coating method [14,15]. The doping concentrations for Ce^{3+} and Tb^{3+} were 10–100 mol% and 6–35 mol% of La^{3+} in $LaMgAl_{11}O_{19}$ host, respectively. Here we take $La_{0.15}Ce_{0.50}Tb_{0.35}MgAl_{11}O_{19}$ film as an example to illustrate the process of film fabrication. 0.0073 g La_2O_3 (99.99%), 0.0651 g $Ce(NO_3)_3 \cdot 6H_2O$, 0.0196 g Tb_4O_7 (99.99%), 0.0302 g $Mg(OH)_2 \cdot 4MgCO_3 \cdot 6H_2O$ (analytical reagent, A.R.), 1.2379 g $Al(NO_3)_3 \cdot 9H_2O$(A.R.) were dissolved in dilute HNO_3 (A.R.) under vigorous stirring, and superfluous HNO_3 was driven off until the pH value of the solution reached between two and three. Then 20 mL water–ethanol (v/v = 1:9, A.R.), 1.6391 g citric acid (A.R.) as chelating agent of metal ions and 2.000 g PEG (molecular weight = 10000, A.R.) as cross-linking agent were added to the solution. Highly transparent sols were obtained after stirring for an hour, which were used for film deposition. The thoroughly cleaned quartz glass substrates with size of 15 mm × 10 mm were dipped into the sols vertically and withdrawn at a speed of 0.5 cm/s. The as-prepared transparent films were dried at 100 °C for an hour to drive off the remaining solvent. The resulted gel films were heated to 500 °C with a heating rate of 1 °C/min and held there for 2 h in air. Finally, the preheated film samples were annealed to 1200 °C at a rate of 5 °C/min and held there for 1 h under the protection of the mixture of nitrogen and hydrogen (5% H_2 + 95% N_2). In order to increase the film thickness, the above-mentioned coating processes were repeated three times.

The left transparent sols were evaporated in an 80 °C water bath to form gels, which were heated to 500 °C and annealed for 2 h. The resulted samples were fully ground, then heated to 1200 °C and held there for 2 h under the protection of the mixture of nitrogen and hydrogen (5% H_2 + 95% N_2).

2.2. Characterization

The X-ray diffraction (XRD) of the powders and films annealed at 1200 °C were examined on a Rigaku-Dmax 2500 diffractometer using Cu$K\alpha_1$ radiation ($\lambda = 0.15405$ nm). Fourier transform infrared spectroscopy (FT–IR) spectra were measured with Perkin-Elmer 580B infrared spectrophotometer with the KBr pellet technique. A thermal analyzer (SDT 2960, TA Instruments) was used to record thermogravimetric and differential thermal analysis (TG–DTA) curves of the gel powders with a heating rate of 10 °C/min under air from room temperature to 800 °C in 100 mL/min and under the mixture of N_2 and H_2 (95% N_2 and 5% H_2) from 800 to 1400 °C in 100 mL/min. The morphology of the crystalline film samples was inspected using an atomic force microscope (AFM, Nanotec Bermad-2000) with tapping mode. The excitation and emission spectra were taken on a Hitachi F-4500 spectrofluorimeter equipped with a 150 W xenon lamp as the excitation source. Luminescence lifetimes were measured on a Lecroy Wave Runner 6100 Digital Oscilloscope (1 GHz) using 350 nm laser (pulse width = 4 ns) as excitation source (Continuum Sunlite OPO). All the measurements were performed at room temperature.

3. Results and discussion

3.1. Formation process and morphology of the films

XRD: The XRD patterns of $La_{0.5}Ce_{0.5}MgAl_{11}O_{19}$ powder samples annealed at different temperatures and film samples annealed at 1200 °C are shown in Fig. 1. It can be found from Fig. 1(a) that the sample annealed at 800 °C is still amorphous. For the sample annealed 900 °C, the diffraction peaks at 19.3°, 32.0°, 37.5°, 45.6°, 60.5° and 66.5° due to Al_2O_3 [18] appeared, which became stronger after annealing at 1000 °C. The diffraction peaks due to LMA appeared after annealing at 1100 °C, and further annealing at 1200 °C led these peaks to become stronger. Similar to the powder sample, well-crystallized LMA film sample appeared after annealing at 1200 °C, as shown in Fig. 1(b). The broad band centered at $2\theta = 22°$ is ascribed to the diffraction of quartz glass substrate (Fig. 1b). The XRD patterns for 1200 °C annealed powder and film samples are in good agreement with the standard JCPDS card for $LaMgAl_{11}O_{19}$ [19]. This indicates that the samples are

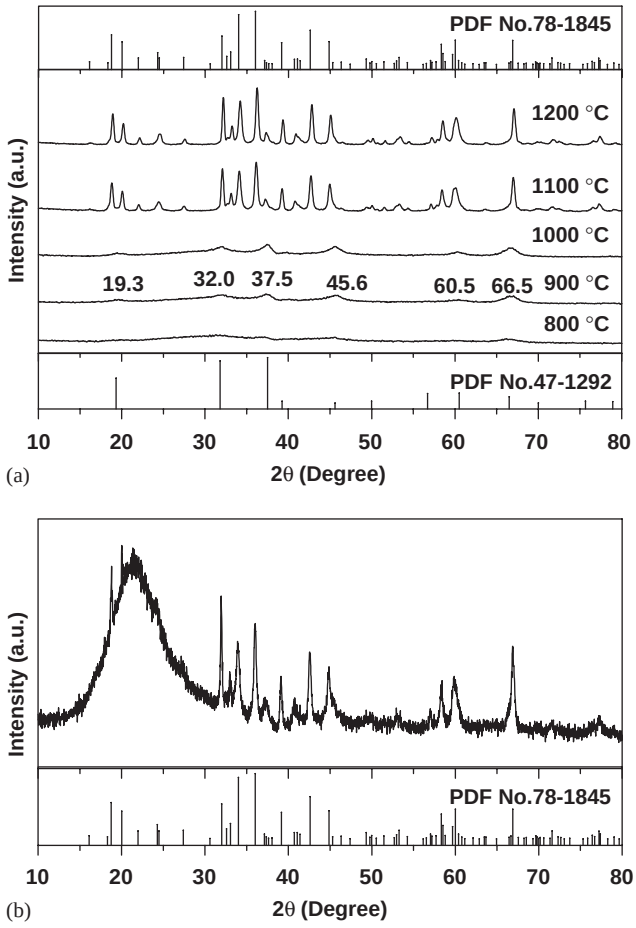

Fig. 1. XRD patterns of $La_{0.5}Ce_{0.5}MgAl_{11}O_{19}$ phosphor powder annealed at different temperatures (a) and film annealed at 1200 °C (b) as well as the JCPDS card of $LaMgAl_{11}O_{19}$ (No. 78-1845) and Al_2O_3 (No. 47-1292).

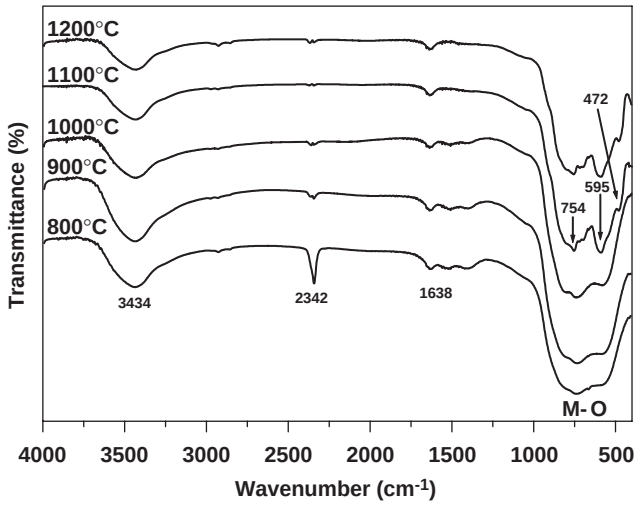

Fig. 2. FT–IR spectra of $La_{0.5}Ce_{0.5}MgAl_{11}O_{19}$ dry gel powders annealed at different temperatures.

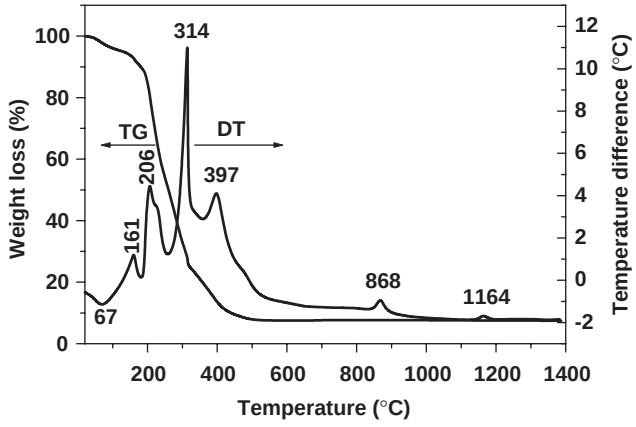

Fig. 3. TG–DTA curves of $La_{0.5}Ce_{0.5}MgAl_{11}O_{19}$ dry gel powder.

well crystallized at 1200 °C, which is about 400 °C lower than that in the traditional solid-state reaction method [20], illustrating the advantage of sol–gel method in lowering the synthesis temperature.

FT–IR spectra: The FT–IR spectra of the powders annealed at different temperature from 800 to 1200 °C are shown in Fig. 2. All the spectra consist of four parts of peaks. The first part peaking at 3434 cm^{-1} originates from the stretching vibration of O–H group of H_2O absorbed by samples during the measurement. The second part at 2342 cm^{-1} is ascribed to the stretching vibration of CO_2 expelled during the combustion of the trapped organic impurities, whose intensity decreases with the increase of annealing temperature. The third part in the range of 1250–1750 cm^{-1} originates from the bending vibration absorption of the –OH groups of H_2O (which is not influenced by the increase of heating temperature as the stretching vibration of OH at 3434 cm^{-1} [15]), the absorption of carbonate groups (1520 cm^{-1}) and NO_3^- groups (1380 cm^{-1}), respectively [21]. The fourth part within the range from 400 to 1000 cm^{-1}, originates from the stretching vibration of $[AlO_4]$ and $[AlO_6]$ [22]. For the samples annealed below 1000 °C, the vibration absorption appeared as an unstructured band. However, for the 1100 and 1200 °C annealed samples, the vibration absorption became more structured. No obvious change was observed for the 1100 and 1200 °C annealed samples, indicating that the sample crystallized almost completely after annealing at 1200 °C. This agrees well with the XRD results.

TG–DTA: In order to verify the crystallization process of the samples further, the dry gel derived from the coating sol, was analyzed by TG–DTA and the results are shown in Fig. 3. The TG curve shows two stages of weight loss. The first one (10 wt%) from 20 to 180 °C, accompanied by an endothermic peak at 67 °C and an exothermic band centered at 161 °C, corresponds to evaporation of water, ethanol and nitric acid and the burnout of ethanol, respectively [15]. The second weight loss (82.5 wt%) occurred from 180 to 500 °C,

accompanied by three exothermic peaks at 206, 314 and 397 °C. The exothermic peak at 206 °C is due to the burnout of excessive citric acid and ethanol and the other two exothermic peaks originates from the burnout of the organic groups in PEG, citric acid and the polyester (formed by the reaction between PEG and citric acid) [15]. No weight loss was observed in the TG curve from 500 to 1400 °C, while two exothermic peaks at 868 and 1163 °C appeared in the DT curve. The first one is due to the crystallization of Al_2O_3 phase, and the second one is attributed to the crystallization of hexagonal $LaMgAl_{11}O_{19}$ phase, agreeing well with the results of the XRD and FT–IR.

AFM and FESEM: AFM was used to characterize the morphology of film annealed at 1200 °C. The planar and stereo AFM images of the film sample are shown in Fig. 4(a) and (b), respectively. It can be seen clearly from the figure that the film is composed homegenous particles with average grain size around 150 nm (Fig. 4a) and a RMS (root mean square) roughness of 4 nm (Fig. 4b).

The thickness of the films deposited on quartz glass was obtained by field emission scanning electronic microscopy (FESEM). The FESEM image of the cross-section of the film sintered at 1200 °C is shown in Fig. 5. It is obvious that the film is crack-free with a thickness of about 340 nm.

3.2. Luminescent properties

$LaMgAl_{11}O_{19}:Ce^{3+}$ films: Ce^{3+}-doped $LaMgAl_{11}O_{19}$ phosphor films show an emission in the UV region. The excitation and emission spectra for $La_{0.5}Ce_{0.5}MgAl_{11}O_{19}$ film are shown in Fig. 6. The excitation spectrum (Fig. 6a) monitored by 350 nm emission consists of a broad band containing of five peaks at 236, 250, 261, 280 (strongest) and 306 nm, which correspond to the electronic transitions from the 4*f* ground state ($^2F_{5/2}$) to the different splitting components of the 5*d* excited state of Ce^{3+}, respectively. The emission spectrum contains a broad band with a maximum at 350 nm, which is ascribed to parity and spin allowed transition from the lowest component of 5*d* (^2D) excited state to the ground state (^2F) of Ce^{3+}. Due to the ground state splitting of Ce^{3+} ($^2F_{5/2}$, $^2F_{7/2}$), an emission tail in the longer wavelength region is observed.

A representative PL decay curve of $La_{0.5}Ce_{0.5}MgAl_{11}O_{19}$ is shown in Fig. 7. This curve can be fitted into a single exponential function as $I = I_0 \exp(-t/\tau)$ (I_0 is the initial intensity at $t = 0$, τ is the $1/e$ lifetime) and the lifetime of Ce^{3+} can be determined by the fitting. The PL intensity and lifetime of $La_{1-x}Ce_xMgAl_{11}O_{19}$ have been studied as a function of Ce^{3+} concentration (x), as shown in Fig. 8. Both the PL intensity and the lifetime of $La_{1-x}Ce_xMgAl_{11}O_{19}$ increase with the increase of concentration of Ce^{3+}(x), and no concentration quenching has been observed. This suggests that the interaction and the energy transfer among the Ce^{3+} ions are negligible, as reported previously [20].

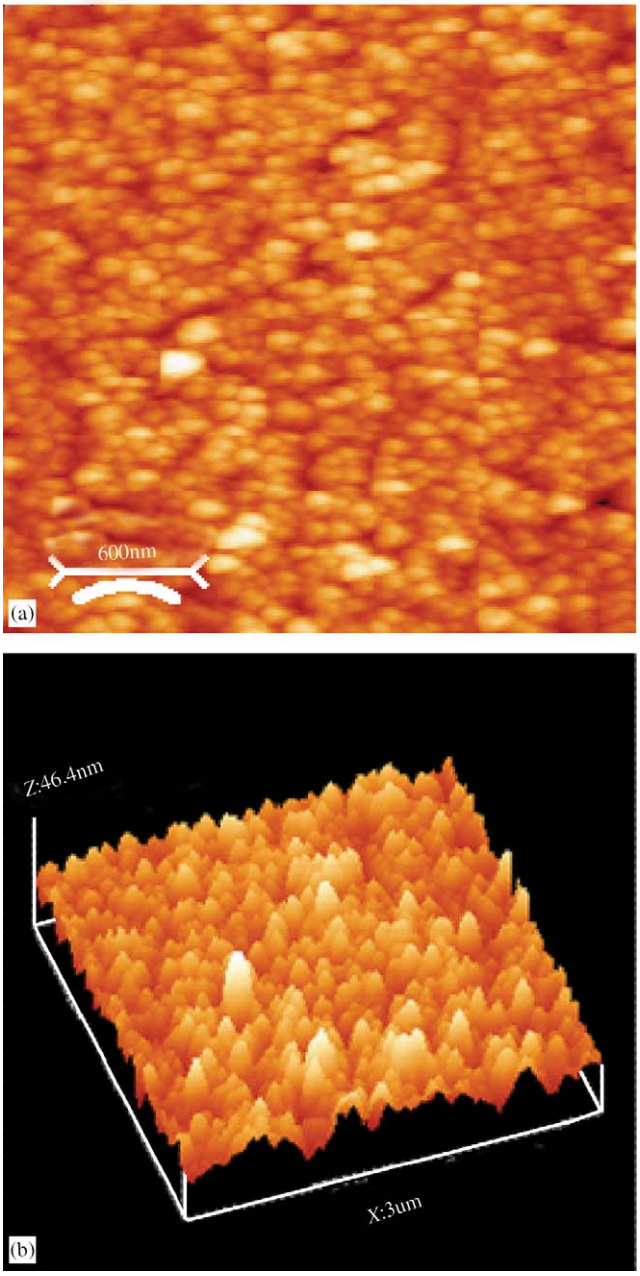

Fig. 4. AFM images of $La_{0.5}Ce_{0.5}MgAl_{11}O_{19}$ film annealed at 1200 °C: (a) planar image and (b) stereo image.

$LaMgAl_{11}O_{19}:Ce^{3+}$, Tb^{3+} films: Ce^{3+} and Tb^{3+}-codoped $LaMgAl_{11}O_{19}$ thin films show strong green luminescence under UV excitation caused by the emission of Tb^{3+}. Fig. 9 shows the excitation (a, b) and emission (c) spectra of $Ce_{0.65}Tb_{0.35}MgAl_{11}O_{19}$ phosphor films. The excitation spectrum monitored by the 542 nm emission ($^5D_4$–$^7F_5$) of Tb^{3+} and 350 nm emission (5*d*–4*f*) of Ce^{3+} are nearly identical to that of

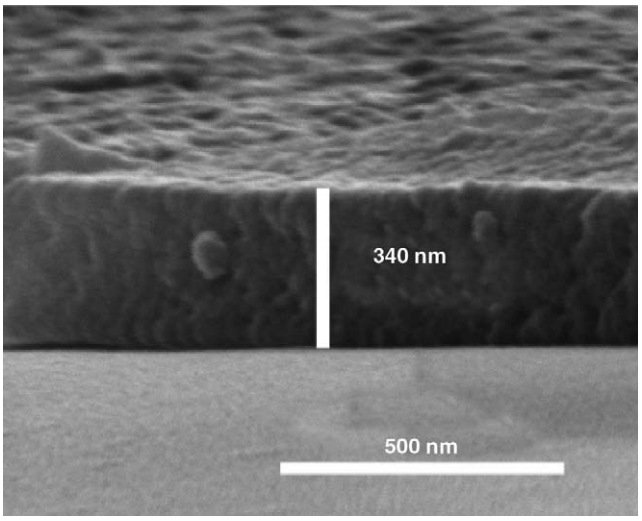

Fig. 5. FESEM image of the cross section of $La_{0.5}Ce_{0.5}MgAl_{11}O_{19}$ film annealed at 1200 °C.

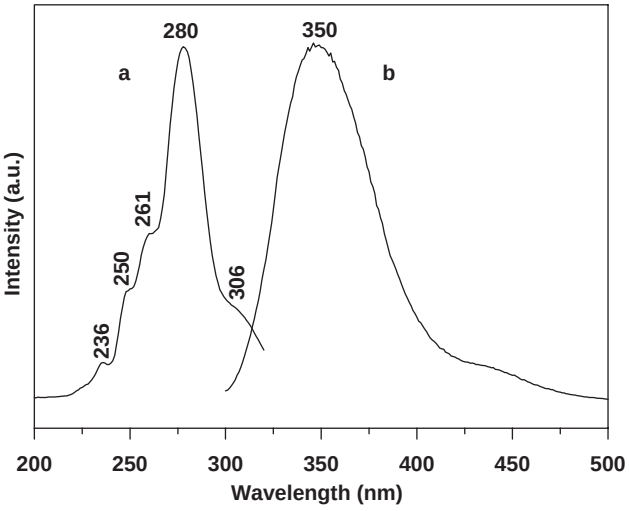

Fig. 6. Excitation (a) ($\lambda_{em} = 350$ nm) and emission spectra (b) ($\lambda_{ex} = 280$ nm) of $La_{0.5}Ce_{0.5}MgAl_{11}O_{19}$ film.

$La_{0.5}Ce_{0.5}MgAl_{11}O_{19}$ (Fig. 6a) except for intensity, suggesting that this excitation is from 4*f*–5*d* transition of Ce^{3+} exclusively. Excitation at 280 nm yields not only the 5*d*–4*f* emission of Ce^{3+}, but also the $^5D_{3,4}$–^7F_J ($J = 6, 5, 4, 3$) emission of Tb^{3+}, as labeled in the figure. Both the excitation and emission spectra indicate that an energy transfer from Ce^{3+} to Tb^{3+} occurs in $Ce_{0.65}Tb_{0.35}MgAl_{11}O_{19}$ film. The energy transfer efficiency from a donor (Ce^{3+}) to an acceptor (Tb^{3+}) can be calculated according to the formula $\eta_{ET} = 1 - I_d/I_0$, where I_d and I_0 are the corresponding integral emission intensity (by calculating the area of the emission spectra) of the donor (Ce^{3+}) in the presence and absence of the acceptor (Tb^{3+}) for the same donor (Ce^{3+}) concentration, respectively [23]. The energy transfer efficiencies

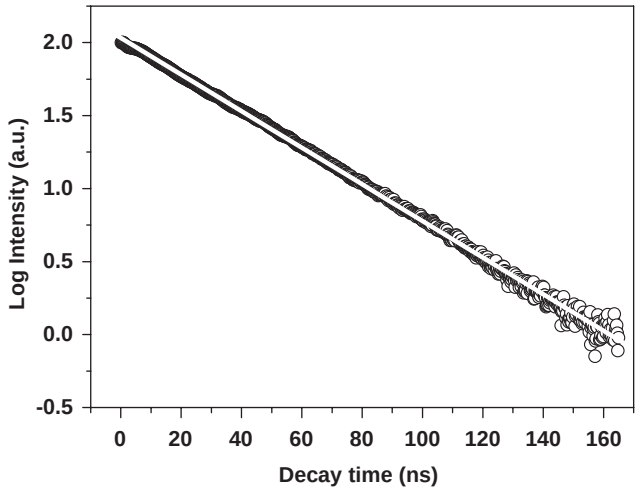

Fig. 7. Decay curve of $La_{0.5}Ce_{0.5}MgAl_{11}O_{19}$ film annealed at 1200 °C ($\lambda_{ex} = 280$ nm, $\lambda_{ex} = 350$ nm) in a logarithmic scale.

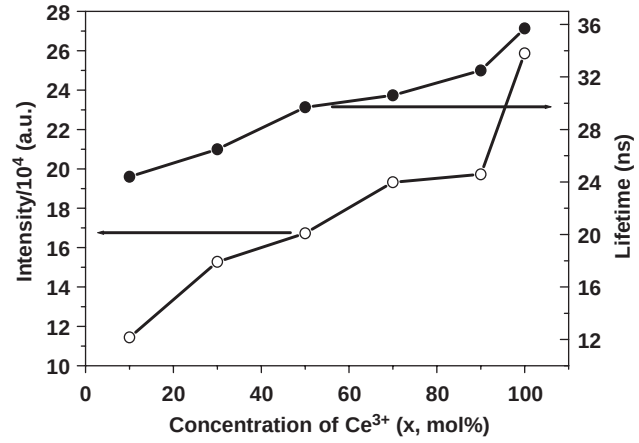

Fig. 8. PL emission intensity and lifetimes of Ce^{3+} as a function of its concentration (x) in crystalline $La_{1-x}Ce_xMgAl_{11}O_{19}$ films.

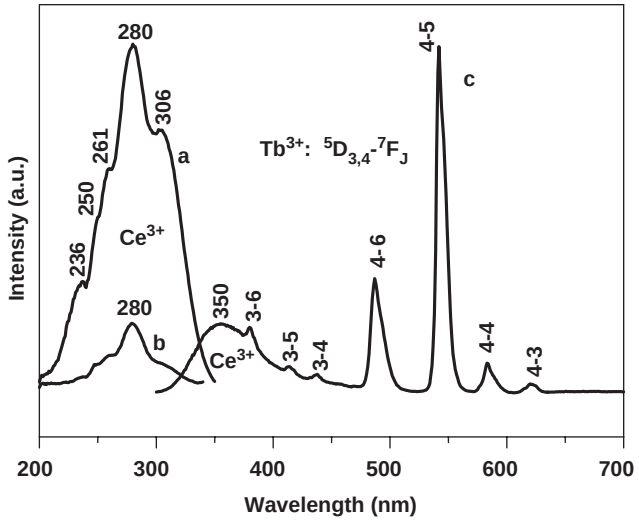

Fig. 9. Excitation (a) ($\lambda_{em} = 542$ nm); (b) ($\lambda_{em} = 350$ nm) and emission (c) ($\lambda_{ex} = 280$ nm) spectra of $Ce_{0.65}Tb_{0.35}MgAl_{11}O_{19}$ film.

Table 1
The energy transfer efficiencies from Ce^{3+} to Tb^{3+} in $La_{1-x-y}Ce_xTb_yMgAl_{11}O_{19}$ as a function of the concentrations of $Ce^{3+}(x)$ and $Tb^{3+}(y)$

	x, y								
	0.5, 0.00	0.65, 0.00	0.5, 0.06	0.5, 0.12	0.5, 0.18	0.5, 0.24	0.5, 0.30	0.5, 0.35	0.65, 0.35
I (Ce^{3+})	124423	186736	91544	70725	66509	55700	47219	43954	31708
I (Tb^{3+})			10593	17870	22382	28348	28937	31701	32502
η_{ET}(%)			26	43	47	55	62	65	83

from Ce^{3+} to Tb^{3+} in $La_{1-x-y}Ce_xTb_yMgAl_{11}O_{19}$ films were studied, as listed in Table 1. It can be found clearly from the table that with the increase of Tb^{3+} concentration (y), the emission intensity of Ce^{3+} decreases, that of Tb^{3+} and the energy transfer efficiencies (η_{ET}) increase. The highest energy transfer efficiency of 65% is obtained for $La_{0.15}Ce_{0.5}Tb_{0.35}MgAl_{11}O_{19}$ film in $La_{0.15}Ce_{0.5}Tb_yMgAl_{11}O_{19}$ series. For comparison, those of $Ce_{0.65}Tb_{0.35}MgAl_{11}O_{19}$ are also listed in Table 1. Obviously, the emission intensity of Ce^{3+} in $Ce_{0.65}Tb_{0.35}MgAl_{11}O_{19}$ is lower than that in $La_{0.15}Ce_{0.5}Tb_{0.35}MgAl_{11}O_{19}$, and the emission intensity of Tb^{3+} in the former is higher than that in the latter. This suggests that a more efficient energy transfer from Ce^{3+} to Tb^{3+} occurs in $Ce_{0.65}Tb_{0.35}MgAl_{11}O_{19}$ than in $La_{0.15}Ce_{0.5}Tb_{0.35}MgAl_{11}O19$. All these results are in agreement with Ref. [23]. The energy transfer efficiency from Ce^{3+} to Tb^{3+} in $Ce_{0.65}Tb_{0.35}MgAl_{11}O_{19}$ was calculated to be as high as 83%. The emission spectrum of $Ce_{0.65}Tb_{0.35}MgAl_{11}O_{19}$ film was compared with that commercial green powder phosphor with the same composition, as shown in Fig. 10. It can be seen that the profile of the two spectra is similar, but the intensity of the film phosphor is only 44% that of commercial powder phosphor. This is due to the thin thickness (350 nm) and waveguide effect in the film phosphor.

Critical distance (R_c) is thought as an important parameter in energy transfer, so we calculated the R_c in $Ce_{0.65}Tb_{0.35}MgAl_{11}O_{19}$ [24,25]. Considering the electric–dipole interaction, $R_c^6 = 0.6 \times 10^{28} \times 4.8 \times 10^{-16} \times f_A \times E^{-4} \times SO$, where oscillator strength f_A (Tb^{3+}) = 10^{-6} (spin forbidden narrow line transitions), E = 3.55 eV (the energy of maximum spectral overlap, maximum of Ce^{3+} emission band), $SO = 0.613\,eV^{-1}$ (the normalized spectral overlap between the excitation lines of Tb^{3+} and the emission of Ce^{3+}), we arrive at $R_c = 0.48$ nm in $Ce_{0.65}$ $Tb_{0.35}MgAl_{11}O_{19}$. This distance indicates that the energy transfer occurs mainly between nearest neighbors of Ce^{3+} and Tb^{3+} [26].

$LaMgAl_{11}O_{19}$ has the magnetoplumbite structure, with a $P63/mmc$ group and lattice parameters $a = 5.58$ Å, $c = 21.94$ Å. In this structure, the large cations La^{3+} (or Ce^{3+}, Tb^{3+}) are located in layers separating spinel-like blocks containing the small cations Al^{3+} and Mg^{2+} [17]. Obviously, the interaction

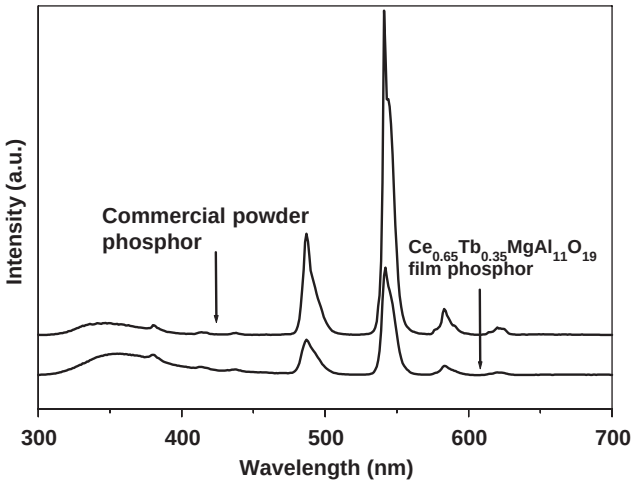

Fig. 10. Emission spectra of $Ce_{0.65}Tb_{0.35}MgAl_{11}O_{19}$ phosphor film and commercial green powder phosphor with the same composition ($\lambda_{ex} = 280$ nm)

of Ce^{3+} and Tb^{3+} in different layers is negligible for their long distance, from which we can conclude that the energy transfer can only occur in the Ce^{3+} and Tb^{3+} within the same layer. In the same layer, the nearest distance between Ce^{3+} and Tb^{3+} is 0.56 nm, the next nearest is 0.96 nm. It can be found that the interaction between Ce^{3+} and the next nearest Tb^{3+} is 1/81 of that between Ce^{3+} and the nearest Tb^{3+}, thus the energy transfer can only occur between Ce^{3+} and the nearest Tb^{3+}. In addition, the lifetime of Tb^{3+} is 10^5 times larger than that of Ce^{3+}. As a result, the emission of Ce^{3+} in LMA host cannot be quenched completely even at high concentration of Tb^{3+}.

The decay curve of Tb^{3+} in $La_{0.15}Ce_{0.50}Tb_{0.35}MgAl_{11}O_{19}$ is shown in Fig. 11. This curve cannot be fitted into a single exponential function, but can into a double exponential function as $I = A_f\exp(-t/\tau_f) + A_s\exp(-t/\tau_s)$, ($\tau_f$ and τ_s are the fast and slow components of the luminescence lifetimes, respectively. A_f and A_s are the fitting parameters.). The average lifetime of Tb^{3+} can be determined by the formula as follows [27]:

$$\tau = (A_f\tau_f^2 + A_s\tau_s^2)/(A_f\tau_s + A_f\tau_s).$$

The decay curve of Ce^{3+} in $La_{1-x-y}Ce_xTb_y$ $MgAl_{11}O_{19}$ is similar to that of $La_{1-x}Ce_xMgAl_{11}O_{19}$

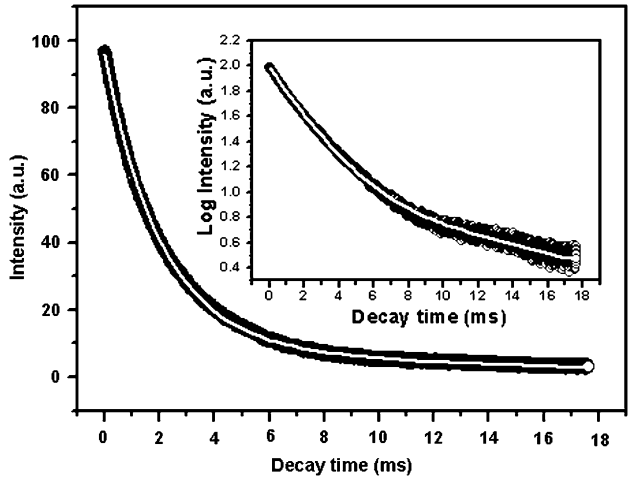

Fig. 11. Decay curve of Tb^{3+} in $Ce_{0.65}Tb_{0.35}MgAl_{11}O_{19}$ film annealed at 1200 °C ($\lambda_{ex} = 280$ nm) in exponential and logarithmic scale.

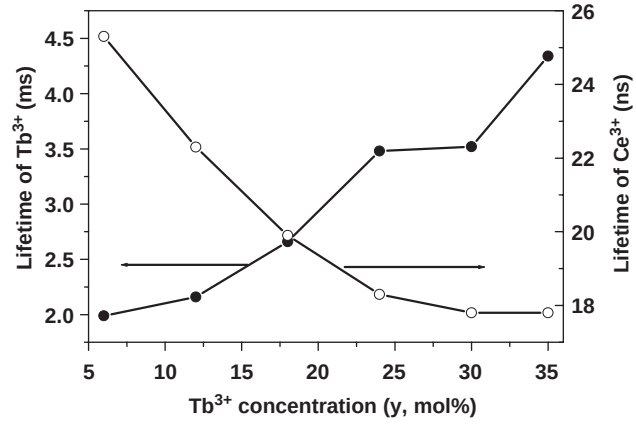

Fig. 12. Lifetimes of Ce^{3+} and Tb^{3+} as a function of Tb^{3+} concentration (y) in crystalline $La_{1-x-y}Ce_xTb_yMgAl_{11}O_{19}$ films.

(Fig. 7), which can also be fitted into a single exponential function of $I = I_0 \exp[-t/\tau]$ and the lifetime can be determined from the fitting. The lifetimes of Ce^{3+} and Tb^{3+} in $La_{1-x-y}Ce_xTb_yMgAl_{11}O_{19}$ are shown in Fig. 12. It can be found from the figure that with the increase of Tb^{3+} concentration, the lifetime of Ce^{3+} in $La_{1-x-y}Ce_xTb_yMgAl_{11}O_{19}$ decreases and that of Tb^{3+} increases due to the energy transfer from Ce^{3+} to Tb^{3+}.

4. Conclusions

$LaMgAl_{11}O_{19}:Ce^{3+}$, Tb^{3+} phosphor films were successively prepared by Pechini sol–gel method using inorganic compounds as main precursors at 1200 °C (400 °C lower than that of the traditional solid-state method for powders). The resulted phosphor films were smooth with a grain size of about 150 nm, RMS roughness of 4 nm and thickness of 340 nm. Energy transfer from Ce^{3+} to Tb^{3+} in $La_{1-x-y}Ce_xTb_yMgAl_{11}O_{19}$ has been observed. Calculation of the energy transfer efficiency shows that $Ce_{0.65}Tb_{0.35}MgAl_{11}O_{19}$ has highest energy transfer efficiency (83%) and strongest green light emission.

Acknowledgments

This project is financially supported by the foundation of "Bairen Jihua" of Chinese Academy of Sciences, the National Natural Science Foundation of China for Distinguished Young Scholars (50225205), and the MOST of China (No. 2003CB314707).

References

[1] J.M. Robertson, M.T. van Tol, Appl. Phys. Lett. 37 (1980) 471.
[2] J.Y. Choe, D. Ravichandran, S.M. Biomquist, D.C. Morton, K.W. Kirchner, M.H. Ervin, U. Lee, Appl. Phys. Lett. 78 (2001) 3800.
[3] S. Park, B.L. Clark, D.A. Keszler, J.P. Bender, J.F. Wager, T.A. Reynolds, G.S. Herman, Science 297 (2002) 65.
[4] K.L. Frindell, M. H Bartl, A. Popitsch, G.D. Stucky, Angew. Chem. Int. Ed. 41 (2002) 960.
[5] Y.E. Lee, D.P. Norton, J.D. Budai, P.D. Rack, M.D. Potter, Appl. Phys. Lett. 77 (2000) 678.
[6] G.R. Bai, H. Zhang, C.M. Foster, Thin Solid Films 321 (1998) 115.
[7] J. Hao, S.A. Studenikin, M. Cocivera, J. Lumin. 93 (2001) 313.
[8] M.B. Korzenski, Ph. Lecoeur, B. Mercey, B. Raveau, Chem. Mater. 13 (2001) 545.
[9] Tc.I. Khristov, N.V. Popovich, S.S. Galaktionov, N.P. Soshchin, Inorg. Mater. 32 (1996) 80.
[10] D. Ravichandran, R. Roy, A.G. Chakhovsoi, C.E. Hunt, W.B. White, S. Erdei, J. Lumin. 71 (1997) 291.
[11] S. Chadha, J.J. Alwan, US Patent (1995) 56 95 809.
[12] P. Rao, Solid State Commun. 99 (1996) 439.
[13] J. Lin, D.U. Sanger, M. Mennig, K. Barner, Mater. Sci. Eng. B 64 (1999) 73.
[14] M.P. Pechini, US Patent 3 330 697, 1967.
[15] M. Yu, J. Lin, Z. Wang, J. Fu, S. Wang, H.J. Zhang, Y.C. Han, Chem. Mater. 14 (2002) 2224.
[16] N. Mermilliod, R. Romero, I. Chartier, C. Garapon, R. Moncorge, IEEE J. Quant. Electron. 28 (1992) 1179.
[17] J.L. Sommerdijk, J.M.P.J. Verstegen, J. Lumin. 9 (1974) 415.
[18] Joint Committee on Powder Diffraction Standards (JCPDS) Card 47-1292
[19] Joint Committee on Powder Diffraction Standards (JCPDS) Card 78-1845
[20] J.M.P.J. Verstegen, J.L. Sommerdijk, J.G. Verriet, J. Lumin. 6 (1973) 425.
[21] M.L. Pang, J. Lin, S.B. Wang, M. Yu, Y.H. Zhou, X.M. Han, J. Phys.: Condens. Matter. 15 (2003) 1.
[22] Junying Zhang, Zhongtai Zhang, Zilong Tang, Zishan Zheng, Yuanhua Lin, Powder. Technol. 126 (2002) 161.
[23] J.C. Bourcet, F.K. Fong, J. Chem. Phys. 60 (1974) 34.
[24] G. Blass, Mater. Chem. Phys. 16 (1987) 201.
[25] G. Blass, Philips Research Reports 24 (1969) 131.
[26] R. Reisfeld, in: J.D. Dunitz et al. (Eds.), Structure and Bonding, 30th edn., Springer, Berlin, New York, 1976, p. 70.
[27] S. Mukarami, H. Markus, R. Doris, M. Makato, Inorg. Chim. Acta. 300–302 (2000) 1014.